



PAPER • OPEN ACCESS

Thermal boundary layers in turbulent Rayleigh–Bénard convection at aspect ratios between 1 and 9

To cite this article: Ronald du Puits *et al* 2013 *New J. Phys.* **15** 013040

View the [article online](#) for updates and enhancements.

Related content

- [Measurements of the instantaneous local heat flux in turbulent Rayleigh–Bénard convection](#)
Ronald du Puits, Christian Resagk and André Thess
- [Resolving the fine-scale structure in turbulent Rayleigh–Bénard convection](#)
Janet D Scheel, Mohammad S Emran and Jörg Schumacher
- [Physical and geometrical properties of thermal plumes in turbulent Rayleigh–Bénard convection](#)
Quan Zhou and Ke-Qing Xia

Recent citations

- [Fluctuations of the wall shear stress vector in a large-scale natural convection cell](#)
R. du Puits and C. Bruecker
- [The ultimate state of convection: a unifying picture of very high Rayleigh numbers experiments](#)
Philippe-E Roche
- [Mean temperature profile and thermal displacement thickness in turbulent Rayleigh–Bénard convection](#)
Tie Wei and Ronald du Puits

Thermal boundary layers in turbulent Rayleigh–Bénard convection at aspect ratios between 1 and 9

Ronald du Puits¹, Christian Resagk and André Thess

Institute of Thermodynamics and Fluid Mechanics, Ilmenau University of Technology, PO Box 100 565, D-98684 Ilmenau, Germany

E-mail: ronald.dupuits@tu-ilmenau.de

New Journal of Physics **15** (2013) 013040 (23pp)

Received 27 July 2012

Published 17 January 2013

Online at <http://www.njp.org/>

doi:10.1088/1367-2630/15/1/013040


Abstract. We report highly resolved temperature measurements in turbulent Rayleigh–Bénard convection in air at a fixed Prandtl number $Pr = 0.7$. Extending our previous work (du Puits *et al* 2007 *J. Fluid Mech.* **572** 231–54), we carried out measurements at various aspect ratios while keeping the Rayleigh number constant. We demonstrate that the temperature field inside the convective boundary layers of both horizontal plates is virtually independent on the global flow pattern accompanying the variation in the aspect ratio. Thanks to technical upgrades of the experimental facility as well as a significant improvement of the accuracy and reliability of our temperature measurement—and unlike in our previous work—we find that the measured profiles of the time-averaged temperature field neither follow a clear power-law trend nor fit a linear or a logarithmic scaling over a significant fraction of the boundary-layer thickness. Analyzing the temperature data simultaneously acquired at both horizontal plates, various transitions in the cross-correlation and the auto-correlation function of the temperature signals are observed while varying the aspect

¹ Author to whom any correspondence should be addressed.



Content from this work may be used under the terms of the [Creative Commons Attribution-NonCommercial-ShareAlike 3.0 licence](https://creativecommons.org/licenses/by-nc-sa/3.0/). Any further distribution of this work must maintain attribution to the author(s) and the title of the work, journal citation and DOI.

ratio Γ . These transitions might be associated with a change in the global flow pattern from a single-roll mode at $\Gamma = 1$ toward a double- or a multi-roll mode pattern at higher aspect ratios.

 Online supplementary data available from stacks.iop.org/NJP/15/013040/mmedia

Contents

| | |
|--|-----------|
| 1. Introduction | 2 |
| 2. The experimental set-up and the measurement technique | 5 |
| 2.1. Experimental facility | 5 |
| 2.2. Measurement technique | 7 |
| 2.3. Experimental procedure | 9 |
| 3. Results | 10 |
| 3.1. Self-similarity of the temperature field | 10 |
| 3.2. Dynamics of coherent structures and the coupling of the boundary layers | 14 |
| 4. Conclusions | 20 |
| Acknowledgments | 21 |
| References | 21 |

1. Introduction

The heat transfer from a hot (cold) solid surface to a surrounding fluid, commonly referred to as thermal convection, plays a key role in many natural flow phenomena as well as in countless technical applications. Since Ludwig Prandtl's famous experiments at the beginning of the last century, we know that the heat transfer coefficient α in Newton's law of cooling $q_c = \alpha(T_s - T_\infty)$, T_s being the surface temperature and T_∞ the fluid temperature, strongly depends on the temperature and the velocity field close to the wall. However, it is still unclear whether or not the structure of the driving (outer) flow may change the temperature field inside this so-called boundary layer. The purpose of the present work is to answer this question performing a series of highly resolved temperature measurements in a large-scale Rayleigh–Bénard (RB) experiment with air at various width-to-height ratios.

Among the heated horizontal or vertical flat plates, the RB set-up is also a very popular model flow to study thermal convection under well-controlled conditions. A fluid layer of depth H is heated from below and cooled from above [1–3], forming convective boundary layers at both horizontal plates. The RB experiment is characterized by the Rayleigh number $Ra = (\beta g \Delta\vartheta H^3)/(\nu\kappa)$, a dimensionless number that quantifies the ratio between buoyancy and inertial forces, and the Prandtl number $Pr = \nu/\kappa$ describing the properties of the fluid. Here, the variables β , g , $\Delta\vartheta$, ν and κ denote the thermal expansion coefficient, the gravitational acceleration, the temperature difference between the hot bottom and the cool top plate, the kinematic viscosity and the thermal diffusivity, respectively. In the case where the fluid layer is laterally confined by sidewalls, the aspect ratio $\Gamma = D/H$, with D being the lateral dimension, has to be added to the set of parameters. For Rayleigh numbers below a critical value Ra_c , the fluid remains at rest and heat is conducted throughout the fluid layer. Exceeding this bound, it starts to move, initiating a convective heat transfer between the horizontal plates. Both, the

heat flux and the velocity of the flow, are quantified by the Nusselt number $Nu = Q_c/Q_d$ and the Reynolds number $Re = \bar{v}H/\nu$, respectively. In these definitions, Q_c and Q_d stand for the convective and the diffusive heat flow and \bar{v} is the typical mean velocity of the flow. In turbulent RB convection, boundary layers are of particular interest since they mainly determine the convective heat transport throughout the fluid layer—one of the fundamental questions when studying RB convection. Previously, scaling laws of the form $Nu = f(Ra, Pr)$ have been established to describe the correlation between the applied input quantities and the resulting heat transport. Considering the great variety of natural or engineering convection phenomena, it quickly becomes obvious that the aspect ratio of the enclosure also plays a crucial role in this process. Whereas many natural flows, such as e.g. atmospheric and oceanic drifts [4], or the motion of the viscous rock in the outer Earth's mantle [5], are confined in a very flat fluid layer, indoor flows [6] or convection in chemical or nuclear reactor chambers take place in enclosures with a rather uniform geometry. Also in many other engineering problems facing a single heated or cooled surface adjoining a virtually infinite fluid layer ($\Gamma \rightarrow 0$), convective boundary layers develop.

RB convection has previously been studied very frequently in samples of $\Gamma \leq 1$ to realize a Ra number as high as possible but keeping the lateral extent of the experiments small [7–10]. In these experiments, the vertical sidewall strongly affects the flow and shapes a large-scale circulation often referred to as the mean flow or wind. In a phenomenological theory, Grossmann and Lohse [11–13] predict the global heat flux and the typical velocity of the convective motion as a function of the input parameters Ra , Pr and Γ . While this theory has proven to be quite successful in providing the global scaling behavior for RB convection at $\Gamma = 1$, it provides only a qualitative prediction for larger aspect ratios [13]. In small aspect ratio cells of the order of unity, it is usually assumed that one convection roll evolves. This roll is the subject of a large variety of dynamic processes such as rotations of the flow plane, cessations or even complete reversals [14–18]. With increasing the aspect ratio, however, this large convection roll breaks down into smaller structures as indicated in various papers in the past. Niemela and Sreenivasan [19] and du Puits *et al* [20] have investigated the structure of the global flow field analyzing local temperature and velocity data. They found clear evidence of significant transitions in the signals and associated these transitions with the evolution of the wind from one shape to another. In a very comprehensive numerical study covering an aspect ratio domain of $0.5 < \Gamma < 12$ and Rayleigh numbers between $10^7 < Ra < 10^9$, Bailon-Cuba *et al* [21] have illustrated the variation in the global flow field very well. In their figure 5, they show flow patterns for aspect ratios $\Gamma = 2.5, 3.0$ and 6.0 demonstrating the transition from a large single- to a multi-roll flow structure. These transitions were accompanied by a variation of 10% in the global Nusselt number. The dependence $Nu(\Gamma)$ in gases with $Pr = 0.7$ has been confirmed experimentally by Fleischer and Goldstein [22] as well as Niemela and Sreenivasan [19]. For higher Prandtl number fluids such as water ($Pr = 4$), Funfschilling *et al* [23] and Sun *et al* [24] reported a weaker change of the order of a few per cent in Nu . Zhou *et al* [25] even found that in a rectangular cell with a base area of $50\text{ cm} \times 15\text{ cm}$ the Nusselt number is independent of the aspect ratio. Again, the authors of this work argued that the weak aspect ratio dependence observed in cylindrical cells is a manifestation of the finite plate conductivity. In a recent numerical study on two-dimensional (2D) RB convection (which, however, may not cover the full dynamical behavior of three-dimensional (3D) RB convection), van der Poel and co-workers [26] explained, by associating characteristic flow structures with the corresponding heat flux, why the aspect ratio dependence of the Nusselt number is more pronounced for small

Prandtl numbers. It is also known that the shape of the sample may affect the heat flux [27–29]. Up to now, it is still unclear whether this variation in the heat flux is caused by boundary layer effects or by the transitions in the structure of the global flow field. The velocity and the temperature fields inside the boundary layers have been studied in detail previously [30–34]. However, most of the experimental works were focused on RB cells of aspect ratio $\Gamma = 1$. In two very recent papers, du Puits *et al* [35, 36] report on highly resolved velocity and temperature measurements at the cooling plate of a large RB experiment at various aspect ratios. They found that the mean profiles of velocity and temperature at the central axis of the experiment are invariant while changing the aspect ratio. But, due to experimental restrictions, they could not study the pure aspect ratio dependence since the variation in Γ has always been accompanied by a change in the Rayleigh number in this series of experiments.

Besides the problem of the self-similarity of the mean temperature profiles with different aspect ratios, there is still no consensus whether or not classical boundary layer models are suited to describe the flow field close to the horizontal plates [3, 34, 37, 38]. One of the prevailing models for not too high Ra numbers is the laminar boundary layer according to Prandtl/Blasius [39, 40]. The main assumptions for this model are, briefly summarized, stationarity, a strict 2D flow with a fixed orientation and a uniform temperature yielding a virtually linear rise of the velocity with increasing the plate distance. For the case where the temperature of the plate (slightly) differs from the fluid temperature, the model has been extended by Pohlhausen [41], who pointed out that the mean temperature follows the same scaling with respect to the plate distance as the mean velocity does. Although it is well known that the flow field in turbulent RB convection contradicts these assumptions, it could be demonstrated in very recent direct numerical simulations that this model seems to be appropriate to describe the velocity and temperature field inside the thermal boundary layer [42, 43]. While the agreement is very good for high Prandtl number fluids such as e.g. water, the deviations are significant for low Prandtl number gases such as e.g. air [38, 43]. Linear temperature profiles of the form $T \sim z$ have been measured by Belmonte *et al* [31] and Lui and Xia [32] by running experiments in water at Ra numbers up to $Ra \approx 10^{10}$. Experimental data for low Prandtl number fluids such as air are rare and mostly date back to a few decades ago. For instance, Townsend [44] and Deardorff and Willis [45] probed the near-wall temperature field using cold wires of the order of $1 \mu\text{m}$ in diameter and 1 mm long. They obtained nonlinear profiles as well, even though their experiments were performed at low Ra numbers. It should be noted here that in all these experiments sensors have been used that are comparable in size with the entire thickness of the boundary layer. Due to this fact the accuracy of those measurements inside the boundary layer was low and it was virtually impossible to discriminate between a linear or a nonlinear scaling. It can be summarized that a large variety of experimental results exist but none of them is convincingly evaluated. Linear temperature profiles mainly obtained in very recent DNS are solely supported by measurements at higher Prandtl numbers but not at lower ones.

A question more related to the dynamics of the flow in turbulent RB convection controversially discussed in the past as well is the effect of the evolution of coherent structures on the heat transport. While, e.g., Villiermaux [46] proposed a model of a delayed ‘coupling of boundary layer instabilities by the slow convective motion of the recirculation’ where these instabilities evolve alternately and periodically at both horizontal plates, Xi *et al* [47] found that they are emitted neither periodically nor alternately from the top and bottom plates.

In the present work, we went beyond the scope of our measurements in the past and performed a new series of simultaneous temperature measurements near the cooling and the heating plates by varying the aspect ratio but keeping the Rayleigh number constant. The Prandtl number was fixed at $Pr = 0.7$. All measurements have been carried out in a large-scale facility called ‘Barrel of Ilmenau’ and cover, within the experimental limits due to the maximum temperature difference, the following parameter domains:

1. $1.13 \leq \Gamma \leq 2.75$, $Ra_1 = 5.2 \times 10^{10}$;
2. $2.75 \leq \Gamma \leq 7.00$, $Ra_2 = 3.8, \dots, 4.0 \times 10^9$;
3. $7.00 < \Gamma \leq 9.00$, $Ra_3 = 1.3 \times 10^9$.

Thanks to an upgrade of the heating system and an optimization of the geometry of the temperature sensor used (details can be found in [48]), the accuracy and the reliability of our temperature measurement have been significantly improved. Using commercial heat flux sensors at the surfaces of the plates close to the location of the temperature sensors, the gradients of the mean temperature at both walls have been verified by this complementary and independent heat flux measurement. In this paper, we wish to answer the following questions.

- Do the aspect ratio and the undoubtedly concomitant transitions in the global flow structure affect the temperature field near the horizontal plates?
- Is there a prevailing scaling relation $\overline{\Theta}(z)$ within the thermal boundary layers in turbulent RB convection in air at $Pr = 0.7$?
- Is there a coupling mechanism between the thermal boundary layers at various aspect ratios?

The paper is organized as follows. In section 2, the experimental facility and the measurement technique are described. In section 3, we discuss the profiles of the mean temperature and the temperature fluctuations close to the horizontal plates as well as the applicability of various scaling laws. Section 4 focuses on correlations of simultaneously acquired temperature signals in both boundary layers, and in section 5 our conclusions are summarized.

2. The experimental set-up and the measurement technique

2.1. Experimental facility

Our measurements have been carried out in a cylindrical RB cell of a fixed diameter $D = 7.15$ m. The working fluid is air with a Prandtl number $Pr = 0.7$ virtually independent of temperature. The fluid is confined between the heated bottom plate and the free-hanging cooling plate as well as a virtually adiabatic sidewall. The bottom plate actually used in the experiment consists of two parts: an electrical underfloor heating system embedded in a 5 cm concrete layer and isolated to the ground with 0.3 m polyurethane plates and an overlay in which water circulates. The water circulation inside this overlay makes the temperature at the surface of the heating plate uniform and balances the differences of the convective heat flux at the plate–air interface. Both layers are thermally coupled by a 2 mm silicon pad. We wish to note here that, compared with our previous work published in [20], the new set-up significantly homogenizes the temperature distribution at the surface of the heating plate (see figure 1). The temperature at the heating plate has been adjusted in a range between $T_h = 31.2$ and 58.2 °C. The deviation of any local

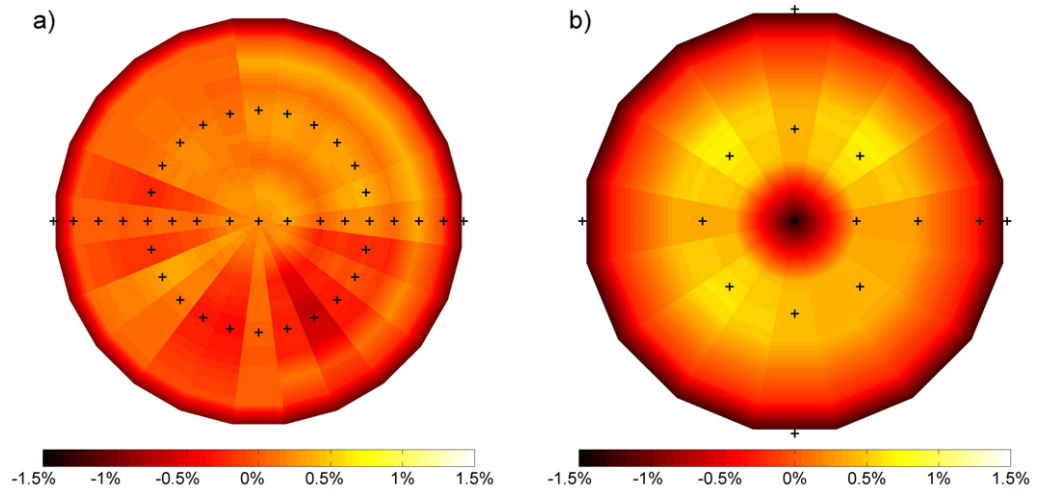


Figure 1. Temperature distribution at the surface of the heating plate (a) and the cooling plate (b) at $T_h - T_c = 35.2$ K, $\Gamma = 2.75$ and $Ra = 5.2 \times 10^{10}$. The plots show the relative deviation $\Delta T_h = 100 [T_h(x, y) - T_h]/[T_h - T_c]$ and $\Delta T_c = 100 [T_c - T_c(x, y)]/[T_h - T_c]$ in per cent of the total temperature drop between the plates. The crosses indicate the position of the internal temperature sensors. The radial temperature distribution at each segment is a projection of the measured distribution along the horizontal line, whereas the angular distributed temperature sensors are used as basic values.

temperature at the surface from the global mean temperature was typically less than $\pm 1\%$ of the total temperature drop between the plates ($\pm 1.5\%$ at the cooling plate). Over the period of one measurement, the mean surface temperature varies in a band ± 0.02 K.

The free-hanging cooling plate consists of 16 segments with water circulation inside as well. The segments are mounted on a solid steel construction and are separately leveled perpendicular to the vector of gravity. The entire construction with a weight of about 6 tons is mounted on a crane and can be lifted up and down. A small gap between the plate and the sidewall required to freely move the plate is hermetically sealed with strips of foam during the experiments. In the present experiments, we set the temperature of the cooling plate between $T_c = 28.8$ and 12.4°C with the same accuracy as indicated for the heating plate. The plate distance has been varied from $H = 6.30$ m to 0.79 m covering aspect ratios between $\Gamma = 1.13$ and 9.00 . The sidewall of the RB cell is shielded by an active compensation heating system to prevent heat exchange with the surroundings. Electrical heating elements are arranged between an inner and an outer isolation of 16 and 12 cm thickness, respectively. The temperature of these elements is controlled to be equal to the temperature at the inner surface of the wall. We have checked the heat loss setting the temperature of both plates to 30.0°C , the fluid temperature that was maintained in the well-mixed bulk region during our experiments. In the case of a perfectly adiabatic side wall, the fluid temperature has to be exactly the same. We have measured 29.9°C , a deviation that indicates a very small heat loss not exceeding 0.5% of the convective heat flux in the experiments. For more detailed information see [20].

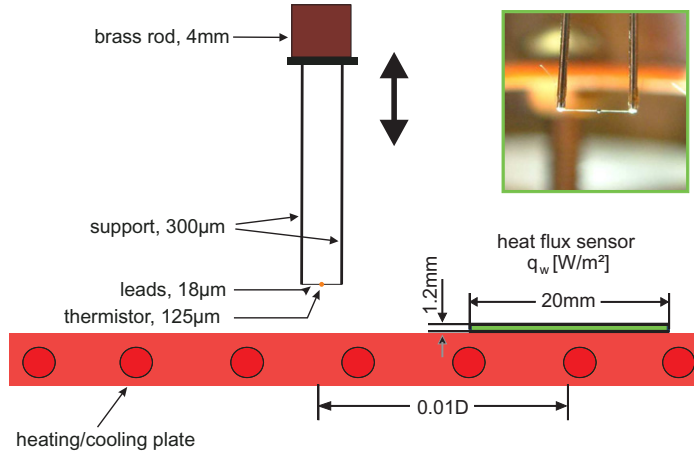


Figure 2. Set-up of the temperature and the heat flux measurement at the heating plate. The temperature sensor can be moved up and down. The heat flux sensor is mounted using a thermally conducting glue. The upper right picture shows a strongly enlarged photograph of the microthermistor and its attachment at the support.

2.2. Measurement technique

Local temperature measurements have been carried out inside and outside the boundary layers. Here, we refer to as *boundary layers* those regions where the temperature increases or decreases from the plate temperature to the temperature of the well-mixed core. It should be noted as well that the typical thickness of this region is of the order of 1 cm in our 6.30 m-high RB cell, at the maximum possible Rayleigh number $Ra = 10^{12}$. Therefore, we used very small, glass encapsulated microthermistors (temperature-dependent resistors) of size $125 \mu\text{m}$ to probe the temperature field. All measurements were carried out along the central axis of the cylindrical RB cell and cover distances between $z \approx 70 \mu\text{m}$ (corresponding to the radius of the microthermistor) and $z \approx 150 \text{ mm}$. The thermistors are connected to the tips of two 0.3 mm supports by $18 \mu\text{m}$ wires (see figure 2). Due to the strong temperature gradients close to the wall and unlike in our experiments in the past [20], we take care to align these connecting wires exactly parallel to the plates and along the iso-surfaces of constant mean temperature in the flow. This prevents measurement errors of the order of a few degrees kelvins [48], and the accuracy particularly very close to the plate surfaces could be improved by a factor of about 20 compared to those measurements in the past. Another source of measurement uncertainty is the spatial averaging of the sensor in the high-temperature gradient flow field close to the wall. This issue may distort (linearize) the natural shape of the temperature field inside the boundary layer. In the work reported here, the maximum gradients have been measured at $\Gamma = 7.01$ and $Ra = 3.79 \times 10^9$. They amount to $d\bar{T}/dz|_{(z=0)} = 8.6 \text{ K mm}^{-1}$ and $d\bar{T}/dz|_{(z=0)} = 9.9 \text{ K mm}^{-1}$ right at the surface of the heating and the cooling plates (see q_h and q_c in table 2). Considering the sensor as a sphere with a diameter of $125 \mu\text{m}$ the temperature drop across the sensor amounts to $\Delta T_s = 1.075 \text{ K}$ and $\Delta T_s = 1.237 \text{ K}$, respectively, or, expressed in units of the total temperature drop across the boundary layer, to $\Delta T_s^* = \Delta T_s / (T_h - T_b) = 0.048$ and $\Delta T_s^* = \Delta T_s / (T_b - T_c) = 0.054$. We wish to note here that these values are the absolute maxima at this particular parameter set, while the temperature drop was significantly smaller during the other measurements.

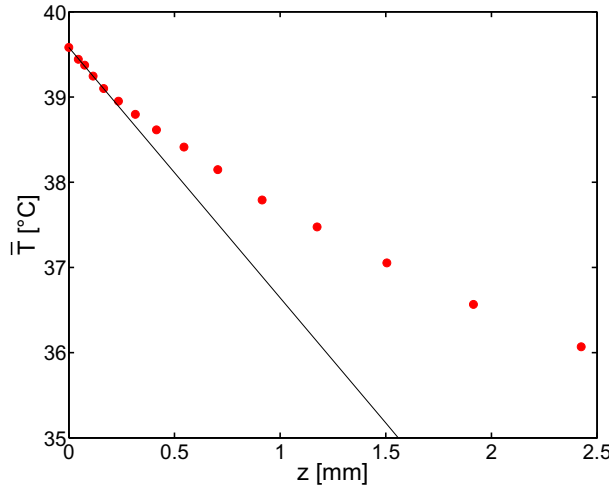


Figure 3. The measured mean temperature profile $\bar{T}(z)$ at the heating plate at $\Gamma = 2.25$ and $Ra = 5.2 \times 10^{10}$ (•, red online). The value $T(z = 0 \text{ mm}) = T_h = 39.583^\circ\text{C}$ is the temperature at the surface of the heating plate. The slope of the black line fits the temperature gradient obtained from the independent measurement of the local wall heat flux (equation (1)).

Before starting the measurements, the sensors were calibrated in a calibration chamber. A resistance temperature detector (RTD) of PT 100 type certified by the Deutsche Kalibrierdienst was used as the reference. The measurement uncertainty of this sensor is specified with 0.02 K in the range between 0 and 100°C . We determined the temperature of the microthermistor in the flow field by measuring its resistance and recomputing the temperature according to the calibration curve. A special bridge with an internal amplifier provides a very low measurement current of $I_{Th} = 5 \mu\text{A}$ sufficiently small to keep the self-heating of the sensor as low as 10 mK. The bridge was connected to a PC-based multi-channel data acquisition system with a resolution of 10^{-4} K and a sampling rate of 200 s^{-1} .

In order to validate the near-wall measurements, heat flux sensors were placed nearby at the plate surface. These sensors with an active area of 3.14 cm^2 provide the local wall heat flux q_w . The temperature drop across the sensors did not exceed 3.5% of the total temperature difference between the plates. According to Fourier's law of heat conduction they permit the calculation of the temperature gradient $d\bar{T}/dz$ at the plate surfaces:

$$\frac{d\bar{T}}{dz} \big|_{(z=0)} = -\frac{q_w}{\lambda} \quad (\lambda \text{ is heat conductivity}). \quad (1)$$

This gradient can be compared with the mean temperature profiles $\bar{T}(z)$ obtained from the microthermistors and provides an idea of how well both measurements coincide. A typical example at an aspect ratio $\Gamma = 2.5$ and an Ra number $Ra = 5.2 \times 10^{10}$ is shown in figure 3. Very close to the wall the mean temperature profile obtained from the thermistor measurement is in excellent agreement with the gradient obtained from the independent heat flux measurement. Starting at $z \approx 0.2 \text{ mm}$ the mean temperature profile deviates from the constant gradient. We are aware of this difference to other measurements in RB convection in water at $Pr \approx 5$ [31, 32] and very recent direct numerical simulations [34, 38, 49] in air at $Pr = 0.7$ that shows linear profiles

Table 1. Set of parameters for the variable aspect ratio measurement series, with Γ and Ra being the aspect ratio and the Rayleigh number, H the plate distance and T_h and T_c the plate temperatures.

| Γ | Ra | H (m) | T_h ($^{\circ}\text{C}$) | T_c ($^{\circ}\text{C}$) |
|----------|-----------------------|---------|------------------------------|------------------------------|
| 1.13 | 5.20×10^{10} | 6.33 | 31.20 | 28.80 |
| 1.25 | 5.18×10^{10} | 5.72 | 31.60 | 28.40 |
| 1.50 | 5.25×10^{10} | 4.77 | 32.80 | 27.00 |
| 1.75 | 5.26×10^{10} | 4.09 | 34.50 | 25.50 |
| 2.00 | 5.26×10^{10} | 3.58 | 36.70 | 23.30 |
| 2.25 | 5.20×10^{10} | 3.18 | 39.50 | 20.50 |
| 2.50 | 5.19×10^{10} | 2.86 | 43.10 | 16.90 |
| 2.75 | 5.20×10^{10} | 2.60 | 47.60 | 12.40 |
| 2.75 | 4.00×10^9 | 2.60 | 31.43 | 28.80 |
| 3.00 | 3.90×10^9 | 2.38 | 31.78 | 28.44 |
| 4.00 | 3.95×10^9 | 1.79 | 34.23 | 26.00 |
| 5.00 | 3.85×10^9 | 1.43 | 37.93 | 22.30 |
| 6.00 | 3.86×10^9 | 1.19 | 43.53 | 16.70 |
| 7.01 | 3.79×10^9 | 1.02 | 58.23 | 13.00 |
| 9.00 | 1.31×10^9 | 0.79 | 45.23 | 15.00 |

over a significant fraction of the boundary layer. However, we believe that our measurements are well verified for the following reasons:

- Each sensor has passed a complex calibration process, resulting in an accuracy of better than ± 10 mK.
- In addition to the profile measurement with the micro-thermistor, the plate temperature at the cell center (see figure 3, $\bar{T}(z = 0 \text{ mm})$) and the temperature in the bulk ($\bar{T}(z \rightarrow \infty)$, not shown) have been measured with two independent temperature probes. The measured values coincide very well.
- The gradient of the mean temperature profile reflects the independently measured local heat flux at the plate surface very well (see figure 3, the full line corresponds to the temperature gradient according to equation (1)).
- The size of the sensor is very small compared with the typical boundary-layer thickness and amounts to only about 1/100 of the latter one.
- The plate surface within a radius of 0.5 m around the measurement position is smooth. The roughness amounts to less than $5 \mu\text{m}$, corresponding to 0.05% of the minimal boundary-layer thickness.

2.3. Experimental procedure

The particular challenge of this experimental work entails studying RB convection at various aspect ratios but keeping the Rayleigh number constant. Unlike in our previous work [35] where a change in the aspect ratio was always accompanied by a variation in the Rayleigh number, here we compensated the latter one by varying the temperature difference $\Delta T = T_h - T_c$ between the plates (see table 1). Moreover, we kept the temperature T_b in the well-mixed bulk constant. Since

this is feasible in experiments only in a limited domain of Γ the full parameter domain is split into the following three ranges:

1. $1.13 \leq \Gamma \leq 2.75$, $Ra_1 = 5.2 \times 10^{10}$;
2. $2.75 \leq \Gamma \leq 7.00$, $Ra_2 = 3.8, \dots, 4.0 \times 10^9$;
3. $7.00 < \Gamma \leq 9.00$, $Ra_3 = 1.3 \times 10^9$.

In this way, we have measured temperature profiles $T(z, t)$ at 14 aspect ratios. Before we started a new measurement, the experiment has run at least 3 days to become stationary. We determined the position $z = 0$ mm according to the following procedure. In a first step, we monitored the visual contact of the sensor with the plate surface using a microscope camera. The position has been refined by checking the electrical contact between the sensor and the conducting plate and we ended up with an accuracy of $\pm 20 \mu\text{m}$. The final adjustment has been obtained after the measurement by shifting the mean temperature profile $\bar{T}(z)$ along the z -axis until it collapses with the plot of the temperature gradient $d\bar{T}/dz$ resulting from the independently measured local heat flux (see figure 3). For each of the profiles, we captured time series of temperature at 35 positions using a finer grid resolution inside the boundary layer and a coarser one outside. In order to estimate the statistical uncertainty of the mean values $\bar{T}(z)$, we estimated the 95% confidence interval. For our 90 min measurement period, the error did not exceed ± 0.1 K even in the transition region between the boundary layer and the bulk where the strongest fluctuations have been observed.

3. Results

3.1. Self-similarity of the temperature field

We start our discussion by presenting profiles of the normalized mean temperature $\bar{\Theta}_h(z) = 2[T_h - T(z)]/[T_h - T_c]$ and $\bar{\Theta}_c(z) = 2[T(z) - T_c]/[T_h - T_c]$ at different aspect ratios. In order to make them comparable, a proper scaling variable for the wall-normal distance z is required. This variable is supposed to compensate for the change in the thermal boundary-layer thickness that accompanies variations of Ra or Γ and permits the evaluation of the pure shape of the profiles. Here, we did not follow the usual practice of using the boundary-layer thickness based on the crossing of the mean temperature gradient at the wall with the asymptotic bulk temperature. Firstly, it is a great challenge to measure this gradient with a sufficiently high accuracy and, secondly, we believe that the thermal displacement thickness δ_t represents a better suited quantity as it takes into account the entire shape of the mean temperature profile and not only the region very close to the wall. Within the measurement domain $0 < z < z_{\max}$ the thermal displacement thickness is defined as

$$\delta_t = \int_0^{z_{\max}} \{1 - \bar{\Theta}(z)\} dz. \quad (2)$$

In figure 4, the displacement thickness δ_t scaled by the plate distance H is plotted. Because of the experimentally limited range of Γ where the Rayleigh number could be kept constant, the diagram is divided into three parts according to section 2.3. For very low aspect ratios of $\Gamma \leq 1.5$, the scatter of the local boundary-layer thickness is relatively strong. This is very close to the critical aspect ratio where a transition from a single- to a double-roll state has been observed [50, 51]. This process is characterized by extremely long time scales of hundreds

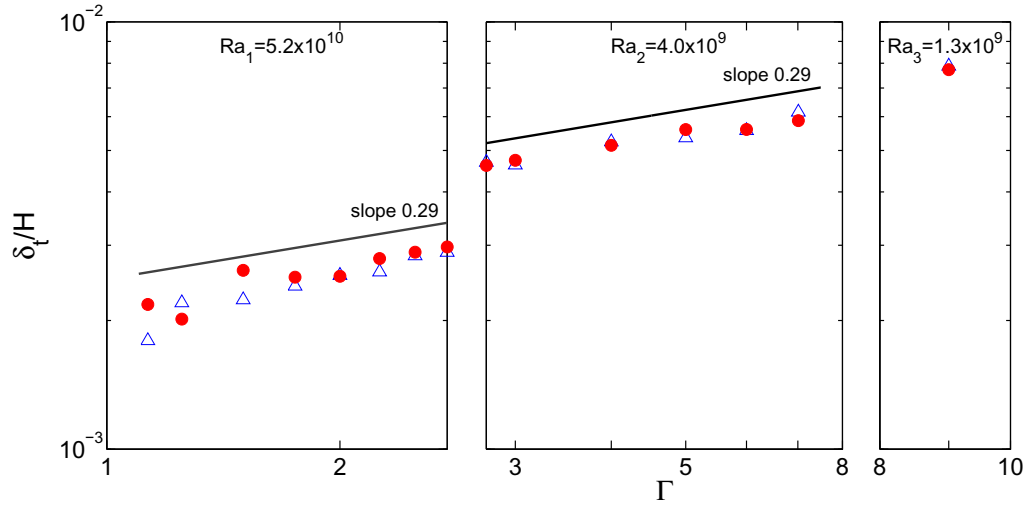


Figure 4. Scaled boundary-layer thickness δ_t/H at the heating (●, red online) and the cooling (△, blue online) plates as functions of the aspect ratio Γ for piecewise constant Rayleigh number.

of eddy turnovers. Thus, it is very likely that the scatter is caused by an insufficiently long averaging time. For higher aspect ratios $\Gamma \geq 2.0$, the data are smoother and the dependence of the boundary-layer thickness on Γ is more distinct. It can be expressed by a power law: $\delta_t/H \sim \Gamma^\gamma$ with a local exponent of $\gamma = 0.29$.

Having found the appropriate scaling quantity δ_t we now turn to the central question of our work: do the local profiles in the center of the heating and cooling plates depend on the aspect ratio? We plot a selection of the normalized mean temperature profiles $\bar{\Theta}(z/\delta_t)$ at aspect ratios between $\Gamma = 1.13$ and 7.00 in figure 5. The full set of data is available online as supplementary material. All profiles obtained at one plate turn out to be similar. The deviation does not exceed 10%. Small deviations visible in the lin–lin representation in the insets might be associated with non-Boussinesq effects due to the change in the temperature drop ΔT (see table 1). It amounts to $\Delta\vartheta = 2.4$ K in the experiment at $\Gamma = 1.13$ and $\Delta\vartheta = 45$ K in the $\Gamma = 7.0$ experiment. While the variation of the fluid properties can be neglected for the minimum temperature difference, it is worthy to note that, e.g., the heat conductivity λ varies by about 15% across the cell for the highest one. This variation causes that the temperature gradients at the surface of the heating and the cooling plates differ by 15% as well. The thermal diffusivity κ and the kinematic viscosity ν vary by even 30%, but to our knowledge there is not any theoretical model or numerical simulation that takes this into account and allows estimation of how this affects the local temperature profiles. Therefore, it cannot be fully ruled out that these small deviations are caused by the variation in the aspect ratio and the global flow pattern, respectively. However, we argue that the deviation is clearly linked to the increasing temperature difference between the plates (the lower curve is for $\Gamma = 1.13$ and $\Delta\vartheta = 2.40$ K; the upper one is for $\Gamma = 7.01$ and $\Delta\vartheta = 45.23$ K; cf table 1), whereas data at a very similar temperature difference but different aspect ratios ($\Gamma = 2.00$, $\Delta\vartheta = 13.40$ K and $\Gamma = 4.00$, $\Delta\vartheta = 8.23$ K) collapse quite well. An influence of the Ra number on the shape of the profiles, however, can be precluded as demonstrated in previous works by Lui and Xia [32], du Puits *et al* [35] and Maystrenko

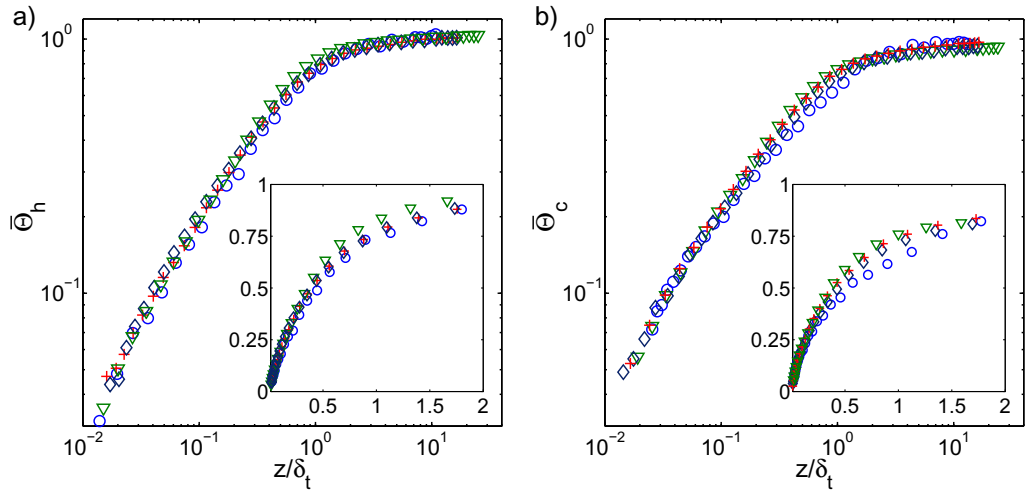


Figure 5. Profiles of the normalized mean temperature $\bar{\Theta}_h(z/\delta_t)$ at the heating (a) and $\bar{\Theta}_c(z/\delta_t)$ at the cooling (b) plates for various aspect ratios $\Gamma = 1.13$ and $Ra = 5.2 \times 10^{10}$ (\circ , blue online), $\Gamma = 2.00$ and $Ra = 5.3 \times 10^{10}$ ($+$, red online), $\Gamma = 4.00$ and $Ra = 3.9 \times 10^9$ (\diamond , black online), and $\Gamma = 7.00$ and $Ra = 3.8 \times 10^9$ (∇ , green online). The insets show the region within the boundary layer in a lin–lin representation. The full set of data is available online as supplementary material (available from stacks.iop.org/NJP/15/013040/mmedia).

et al [52]. At first glance, the self-similarity of the profiles is surprising. Based on the concept of one large single roll at an aspect ratio of about unity, it was expected that the distinct shear layer at the surface of the horizontal plates vanishes and the structure of the temperature (and the velocity) field inside the boundary layer changes when the single roll breaks down into smaller structures. Obviously, this is not the case. Now one may argue that the motion of the large-scale circulation in RB samples of cylindrical shape is a very complicated interference of a large variety of basic flow modes with different time scales [51]. Also, the visualization of the global flow using cloudlets of fog [53] or applying the shadowgraph technique [54] does not show a singular orientation of the flow over at least one eddy turnover time. Considering the strongly varying time scales of the horizontal velocity and its orientation in the vicinity of the cooling plate [55], we conclude that the simple model of one single-roll structure might be insufficient to describe the large-scale motion in cylindrical RB cells of aspect ratio 1. In fact, the convective flow is a collection of smaller fluid structures such as eddies, twistors, plumes and other varieties that move along the plates permanently changing the orientation of the local flow vector. This chaotic flow with at least two significant velocity components creates boundary layers strongly different from the model of a Prandtl/Blasius shear layer, which implies a well-oriented incident flow with only one predominant and temporally stable velocity component. Following this idea, one would expect also the observed deviation of the measured mean temperature profile from Pohlhausen's model. It seems to be easy to carry over this idea to higher aspect ratios and to explain the conservation of the mean temperature profiles with it.

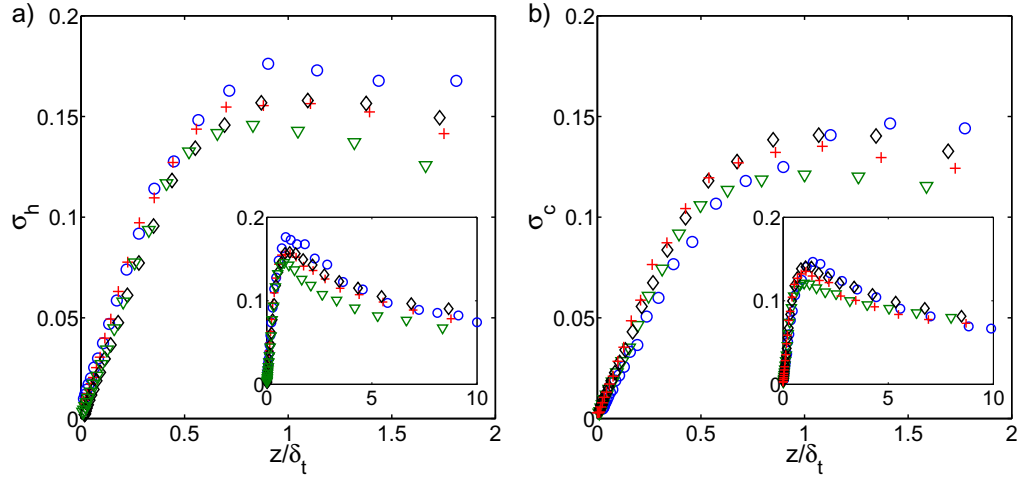


Figure 6. Profiles of the rms temperature fluctuations $\sigma_h(z/\delta_t)$ at the heating (a) and $\sigma_c(z/\delta_t)$ at the cooling (b) plates for various aspect ratios $\Gamma = 1.13$ and $Ra = 5.2 \times 10^{10}$ (\circ , blue online), $\Gamma = 2.00$ and $Ra = 5.3 \times 10^{10}$ ($+$, red online), $\Gamma = 4.00$ and $Ra = 3.9 \times 10^9$ (\diamond , black online), and $\Gamma = 7.00$ and $Ra = 3.8 \times 10^9$ (∇ , green online). The insets show the entire domain. The full set of data is available online as supplementary material (available from stacks.iop.org/NJP/15/013040/mmedia).

Next, we wish to check whether the profiles of the root-mean-square (rms) temperature fluctuations expressed as

$$\sigma(z) = \frac{2}{\Delta T} \left\{ \frac{1}{N-1} \sum_{i=1}^N [T_i(z) - \bar{T}(z)]^2 \right\}^{1/2}, \quad (3)$$

where $\bar{T}(z)$ is the mean temperature—also remain unchanged with increasing the aspect ratio as well. In figure 6, we plot $\sigma(z/\delta_t)$ for the same selection of aspect ratios between $\Gamma = 1.13$ and 7.00 as done before. We would like to focus our discussion on the rising slope of the profiles. The gradient $\partial\sigma/\partial(z/\delta_t)$ remains constant up to 70% of the maximum of the fluctuations and is virtually equal for all aspect ratios. The position of the maxima coincides fairly well with $z/\delta_t = 1$, supporting that the displacement thickness is a well-suited basis to judge about the conservation of the typical flow field. The position of the maxima corresponds as well with the position where about 70% of the maximum temperature drop across the boundary layer is reached, which is in good agreement with early measurements in water reported by Tilgner *et al* [56] and Lui and Xia [32].

Having discussed the self-similarity of the mean temperature profiles and its fluctuations, we turn to our second question expressed in section 1: do the mean temperature profiles $\bar{\Theta}(z/\delta_t)$ correspond to a linear, logarithmic or a power-law scaling function? The redesigned temperature sensor improving the accuracy and the reliability of the measurement by a factor of about 10 enables us to apply the following diagnostic functions:

$$X = \frac{d\bar{\Theta}}{d(z/\delta_t)}, \quad (4)$$

$$Z = \frac{d\bar{\Theta}}{d[\log(z/\delta_t)]}, \quad (5)$$

$$\Xi = \frac{d[\log(\bar{\Theta})]}{d[\log(z/\delta_t)]}. \quad (6)$$

In the case where one of the scalings fits a certain fraction of the profiles, the curves exhibit a pronounced plateau. The scaling functions $X(z/\delta_t)$, $Z(z/\delta_t)$ and $\Xi(z/\delta_t)$ applied to our profiles at the heating and the cooling plates are plotted in figure 7. The upper plots (figures 7(a) and (b)) show the diagnostic function $X(z/\delta_t)$. A linear fraction is completely missing except very far from the wall where the temperature gradient asymptotically goes to zero. Very close to the wall, the function tends to become a constant, indicating the existence of a viscous sub-layer with a linear temperature gradient. However, even when using the smallest sensors of $125 \mu\text{m}$ in our large-scale experiment, this layer remains unresolved. Analyzing $Z(z/\delta_t)$ and $\Xi(z/\delta_t)$ (see figures 7(c)–(f)), it is possible to detect neither a logarithmic scaling as proposed for a turbulent boundary layer [2] nor a power-law scaling over a broad region of the boundary layer. However, the latter one seems to be the best fit that we already have for the region $0.05 < z/\delta_t < 0.4$. Compared to our temperature measurements in the past [35], the application of the diagnostic functions permits a more precise analysis of the data points than the simple regression function as used in our previous work.

Summarizing the results in this section it can be stated that the variation of the aspect ratio and the concomitant transition in the global flow structure does not affect the temperature field close to the heating and the cooling plates. We demonstrated as well that a power law might be the best fit for the region $z < 0.4\delta_t$ within the thermal boundary layer. The rms temperature fluctuations rise linearly to a maximum that is located very close to the displacement thickness δ_t of the thermal boundary layer.

We have listed a summary of the data in numerical form in table 2. The collection is completed by local Nusselt numbers $Nu_{l,h}$ and $Nu_{l,c}$ that have been discussed in detail in [57].

3.2. Dynamics of coherent structures and the coupling of the boundary layers

In this subsection, we will focus particularly on two specific questions that are closely related to the dynamics of coherent boundary layer structures.

- Is the generation of coherent structures as an instability of the convective boundary layer rather a random or a periodic process?
- Are the boundary layers at the top and the bottom plates coupled by these coherent structures and the large-scale circulation?

Since coherent structures are generated in a region adjacent to the thermal boundary layer, we analyzed temperature time series at an arbitrarily chosen distance of $7\delta_t$. We computed the autocorrelation function C_{xx} of the discrete time series $T(z, t)$ with a time step τ between subsequent temperature samples $T(n)$ and $T(n+1)$. The function is defined in its normalized form as

$$C_{xx}(m) = \frac{1}{N} \sum_{n=1}^{N-m+1} T'(n) \cdot T'(n+m-1). \quad (7)$$

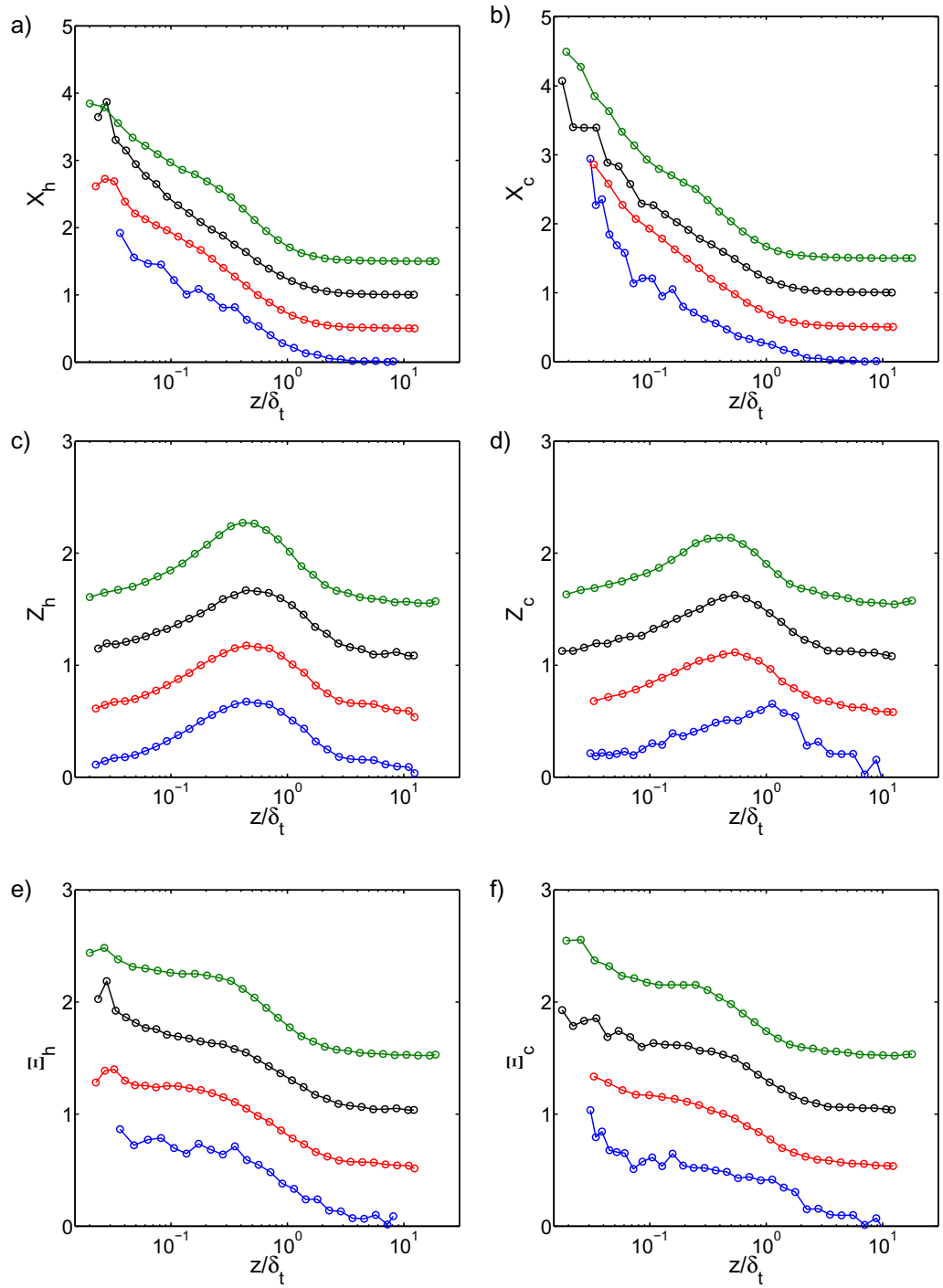


Figure 7. Diagnostic functions X , Z and Ξ applied to the mean temperature profiles at the heating (a,c,e) and the cooling (b,d,f) plates for aspect ratios $\Gamma = 1.13$ (blue online), $\Gamma = 2.00$ (red online), $\Gamma = 4.00$ (black online), and $\Gamma = 7.00$ (green online). In all diagrams, data sets for various aspect ratios are shifted by +0.5 each. They are ordered from the bottom $\Gamma = 1.13$ to the top $\Gamma = 7.00$.

Table 2. Results of the variable aspect ratio measurement series, where Γ and Ra are the aspect ratio and the Rayleigh number, q_h and q_c denote the dimensional heat flux at the center of the heating and the cooling plates and $Nu_{l,h}$ and $Nu_{l,c}$ are the corresponding Nusselt numbers [57], and $\delta_{t,c}$ and $\delta_{t,h}$ are the displacement thicknesses of the thermal boundary layers.

| Γ | Ra | q_h (Wm ⁻²) | q_c (Wm ⁻²) | $Nu_{l,h}$ | $Nu_{l,c}$ | $\delta_{t,h}/H$ | $\delta_{t,c}/H$ |
|----------|-----------------------|---------------------------|---------------------------|------------|------------|------------------|------------------|
| 1.13 | 5.20×10^{10} | 9.3 | 8.1 | 901 | 780 | 0.002 18 | 0.001 79 |
| 1.25 | 5.18×10^{10} | 12.0 | 11.9 | 924 | 841 | 0.002 02 | 0.002 20 |
| 1.50 | 5.25×10^{10} | 22.5 | 23.6 | 995 | 938 | 0.002 62 | 0.002 24 |
| 1.75 | 5.26×10^{10} | 36.7 | 42.7 | 1057 | 1033 | 0.002 53 | 0.002 41 |
| 2.00 | 5.26×10^{10} | 55.7 | 66.8 | 1098 | 1082 | 0.002 54 | 0.002 55 |
| 2.25 | 5.20×10^{10} | 79.7 | 98.9 | 1131 | 1126 | 0.002 79 | 0.002 60 |
| 2.50 | 5.19×10^{10} | 114.5 | 139.2 | 1178 | 1158 | 0.002 89 | 0.002 84 |
| 2.75 | 5.20×10^{10} | 162.8 | 189.9 | 1247 | 1177 | 0.002 97 | 0.002 89 |
| 2.75 | 4.00×10^9 | 7.5 | 10.3 | 763 | 878 | 0.004 61 | 0.004 69 |
| 3.00 | 3.90×10^9 | 8.5 | 15.0 | 718 | 907 | 0.004 74 | 0.004 62 |
| 4.00 | 3.95×10^9 | 28.6 | 40.0 | 931 | 1063 | 0.005 14 | 0.005 24 |
| 5.00 | 3.85×10^9 | 64.4 | 80.4 | 1064 | 1133 | 0.005 60 | 0.005 35 |
| 6.00 | 3.86×10^9 | 126.0 | 139.1 | 1160 | 1234 | 0.005 60 | 0.005 57 |
| 7.01 | 3.79×10^9 | 245.9 | 249.9 | 1318 | 1318 | 0.005 87 | 0.006 15 |
| 9.00 | 1.31×10^9 | 151.0 | 152.7 | 1174 | 1276 | 0.007 73 | 0.007 88 |

In this equation, $T'(n) = T(n) - \bar{T}$ represents the zero-mean temperature fluctuations measured at the (cold) top and the (hot) bottom plates. In figures 8(a)–(d), the autocorrelation function is plotted for a selection of aspect ratios between $\Gamma = 1.13$ and 7.00.

At $\Gamma = 1.13$ (see figure 8(a)), $C_{xx}(\tau)$ rapidly decrease to zero, indicating that temperature fluctuations occur randomly and coherent structures do not evolve in a periodic manner. This is a confirmation of previous measurements in cells of this geometry by Xi *et al* [47] and du Puits *et al* [20] and contradicts the model of Villiermaux. This observation holds as well for the highest aspect ratio $\Gamma = 7.00$ as shown in figure 8(d). At aspect ratio $\Gamma = 2.00$ (figure 8(b)) periodic oscillations are significant in the temperature signals at both plates. The typical cycle time is $\Delta\tau = 180$ s, but both signals are correlated over a much longer period of more than 1.500 s. In order to compare the correlations with the large-scale dynamics of the flow, we estimate the typical eddy turnover time t_e using velocity data from previous measurements [36]. With a typical wind velocity of $v = 0.35$ m s⁻¹ at $Ra = 5.2 \times 10^{10}$ and $\Gamma = 2.00$, we obtain $t_e = (2D + 2H)/v = (2 \times 7.15$ m + 2×3.58 m)/ 0.35 m s⁻¹ = 61.3 s at a rectangular path along the side walls. The correlation time $\Delta\tau = 180$ s is three times longer than t_e indicating that coherent structures emerging from the boundary layers may not be the trigger of these temperature oscillations. We associate the observed oscillations with a decay of the single-roll flow mode at aspect ratio $\Gamma = 1.13$ into a mode with at least two convection rolls at aspect ratio $\Gamma = 2.00$ (see the inset of figure 8(b)). Over time, the location of the rolls with reference to the cell axis varies with the result that a hot fluid from the bottom plate or a cold fluid from the top plate alternatively hit the temperature sensor, generating the observed periodic oscillations. Increasing the aspect ratio again to $\Gamma = 4.00$ (see figure 8(c)) the type of

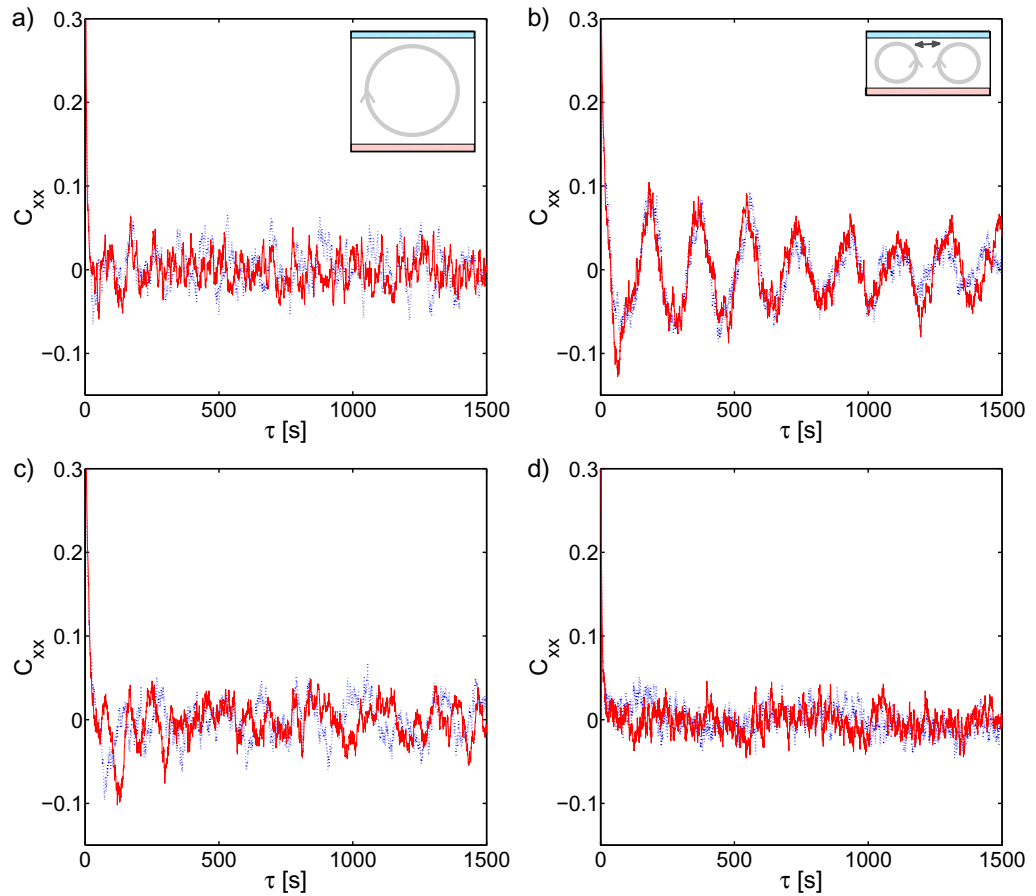


Figure 8. Autocorrelation function $C_{xx}(\tau)$ of the temperature time series $T(z, t)$ at a relative distance $z/\delta_t \approx 7$ from the heating plate (full line, red online) and the cooling plate (dotted line, blue online) for various aspect ratios; (a) $\Gamma = 1.13$ and $Ra = 5.2 \times 10^{10}$, (b) $\Gamma = 2.00$ and $Ra = 5.3 \times 10^{10}$, (c) $\Gamma = 4.00$ and $Ra = 3.9 \times 10^9$ and (d) $\Gamma = 7.00$ and $Ra = 3.8 \times 10^9$. The insets in (a) and (b) show hypothetical sketches of the global flow structure for the respective aspect ratio.

correlation changes again. The periodic oscillations in the autocorrelation function vanish and only a short-term correlation with a delay time $\Delta\tau = 75$ s survives. Assuming that at higher aspect ratios, convection rolls with a typical diameter of the plate distance $H = 1.79$ m and a typical velocity of $v = 0.189$ m s⁻¹ establish [36], the eddy turnover time amounts to $t_e = 29.7$ for this specific case. This is still much shorter than the correlation time and a similar mechanism as in the $\Gamma = 2.00$ cell may act. Summarizing at this point, we conclude that in RB cells of a cylindrical shape at $Pr = 0.7$ and a sufficiently high Ra number coherent structures are randomly generated. The observed periodicity in the temperature time signals at aspect ratios $2 \leq \Gamma \leq 4$ is rather due to the relative motion of the large-scale structures with reference to the location of the sensor.

Simultaneous temperature measurements at the center of the heating and the cooling plates also permit studying the coupling of the boundary layers by coherent structures or the large-scale circulation. From a physical point of view, two possible scenarios may exist: (i) coherent

structures such as thermal plumes having been generated close to one of the plates travel along with the large-scale circulation and arrive at the opposite plate. Here, they induce an instability of the boundary layer, a new coherent structure develops and the process repeats. We refer to this scenario as coupled boundary layers. (ii) Coherent structures emerging from one of the boundary layers are fully mixed in the bulk region and never attain the opposite plate that decouples the boundary layers. We are particularly focusing on how this depends on the plate distance and aspect ratio, respectively. To this end, we computed the normalized cross-correlation function of simultaneously measured time series at the heating and the cooling plates defined as

$$C_{xy}(m) = \frac{1}{N} \sum_{n=1}^{N-m+1} T'(n) \cdot T''(n+m-1), \quad (8)$$

where T' and T'' denote the zero-mean temperature fluctuations at the bottom and at the top plate, respectively.

The upper line charts in each of the four sub-frames in figure 9 represent the cross-correlation of the temperature time signals at the specific distance $z = 150$ mm or $z/\delta_t \approx 10$ from the heating and the cooling plates, respectively. They show whether or not temperature fluctuations appearing in the vicinity of the bottom boundary layer are measurable at the same position with reference to the top boundary layer and vice versa. Furthermore, they give an idea of the time delay between the signals. Basically, as shown in the figures we found three different types of correlation between the temperature signals in the domain of Γ and Ra investigated here. The first one is that the signals are completely uncorrelated (as can be seen in figure 9(a) for $\Gamma = 1.13$, $Ra = 5.2 \times 10^{10}$). The second type of correlation exhibits periodic oscillations with a long cycle time with reference to the eddy turnover time. These oscillations hold over a very long period virtually as long as the full measurement time at each of the positions (see figure 9(b), $\Gamma = 2.00$, $Ra = 5.3 \times 10^{10}$). Finally, a third type has been found that is characterized by one single peak and with a short delay time (see figures 9(c) and (d), $\Gamma = 4.00$, $Ra = 3.9 \times 10^9$ and $\Gamma = 7.00$, $Ra = 3.8 \times 10^9$). In the following, we will discuss these observations and we will try to associate them with certain flow scenarios within the convection sample. However, it has to be noted at this point that a substantiated discussion on this topic would require a measurement of the entire 3D velocity field inside the RB cell, which is not possible in our experiment at the moment.

In the case of aspect ratio $\Gamma = 1.13$, the cross-correlation function C_{xy} tends to zero for all τ . The signals are uncorrelated and coherent structures do not survive on the way from one plate to the other. At $\Gamma = 2.00$, strong periodic correlations similar to the autocorrelation function are visible. The cycle time amounts to $\Delta\tau = 180$ s, which is three times longer than the eddy turnover time. They are in accordance with the period obtained from the autocorrelation function C_{xx} of the signal. As already discussed before, this correlation is caused by the relative motion of large-scale structures with respect to the location of the sensors and is not due to a coupling of the boundary layers by small coherent structures. While the temperature fluctuations at the heating and the cooling plates are in phase for aspect ratios between $\Gamma = 2$ and 4, they get out of phase decreasing the plate distance again. The delay time amounts to $\Delta\tau = 6.5$ s for $\Gamma = 7.00$ ($H = 0.90$ m) and $Ra = 3.79 \times 10^9$. Assuming that convection rolls with a diameter of the order of the plate distance fill the space between the horizontal plates, the typical path length of a small coherent structure from one plate to the other is $l = \pi H/2 = \pi 0.90 \text{ m}/2 = 1.41$ m. With a typical velocity of $v = 0.189 \text{ m s}^{-1}$ [36], the time required for a specific event to reach the opposite plate amounts to $t = l/v = 1.4 \text{ m}/0.189 \text{ m s}^{-1} = 7.4$ s. This is very close to the

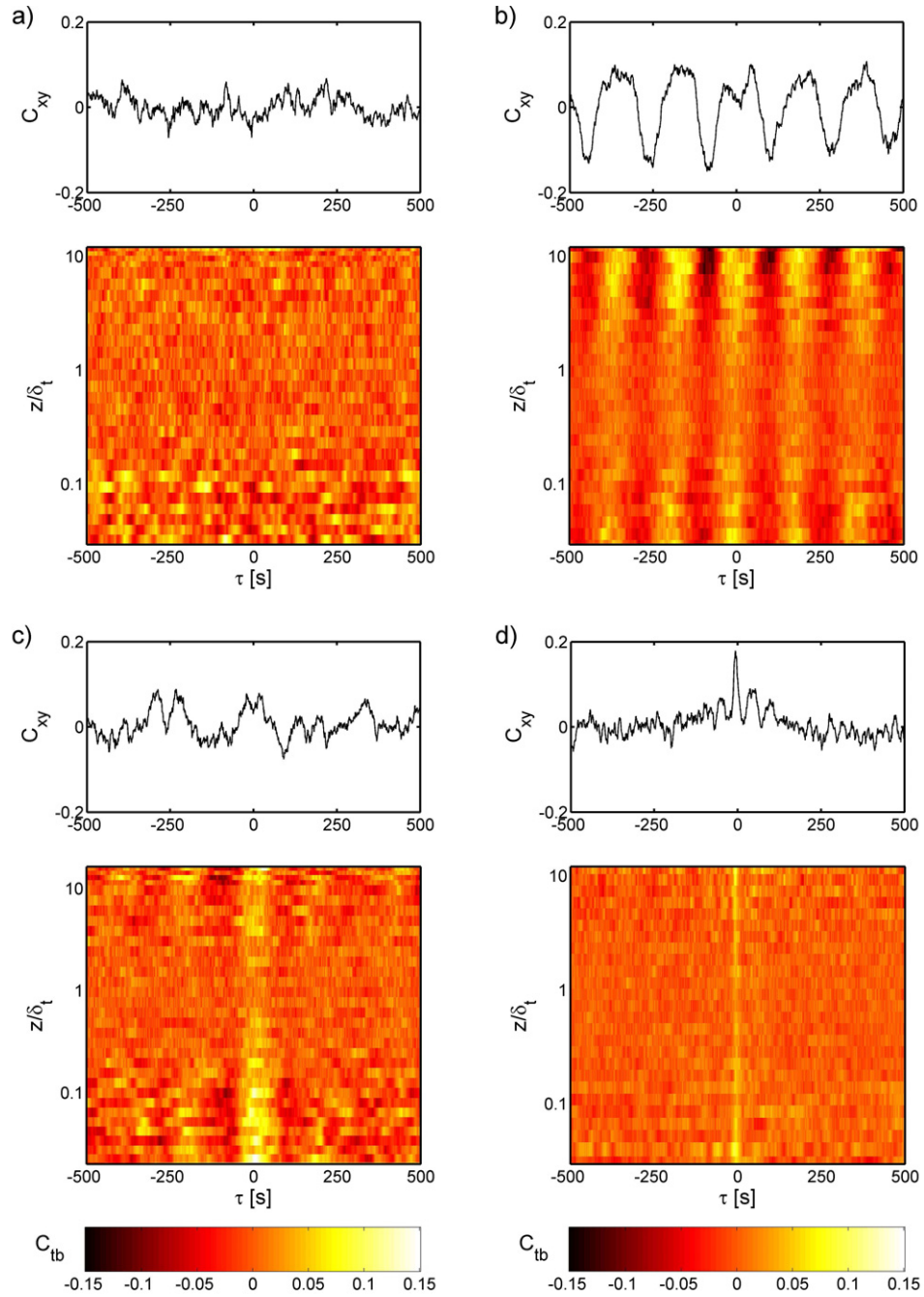


Figure 9. The cross-correlation function $C_{xy}(\tau)$ of the simultaneously measured temperature time series $T(z, t)$ at the heating and the cooling plates for various aspect ratios: (a) $\Gamma = 1.13$ and $Ra = 5.2 \times 10^{10}$, (b) $\Gamma = 2.00$ and $Ra = 5.3 \times 10^{10}$, (c) $\Gamma = 4.00$ and $Ra = 3.9 \times 10^9$ and (d) $\Gamma = 7.00$ and $Ra = 3.8 \times 10^9$. The upper line chart of each sub-frame shows the correlation at the maximum distance $z_{\max} = 150$ mm between the sensor and the plate. The lower graph shows $C_{xy}(\tau, z/\delta_t)$. Each of the lines represents the color-coded cross-correlation function at one specific distance z/δ_t .

correlation time and indicates that with increasing the aspect ratio the boundary layers become coupled.

Finally, we wanted to check how deep into the boundary layer these correlations can be detected. To this end, we plot a composition of the cross-correlation at all 35 measurement positions z in the lower diagram of each sub-frame of figures 9(a)–(d). One horizontal color-coded bar in the graph represents the cross-correlation function $C_{xy}(\tau)$ at the specific position z/δ_t . The upper bar corresponds to the correlation of the sensor signals at the maximum distance $z = 150$ mm from both horizontal plates and represents the same data as shown in the line plot. The lower bar shows the correlation of the sensor signals if both temperature probes are located at their minimum distance from the surface of the plates. It is interesting to note that for all parameters of Γ and Ra , correlations outside the boundary layers at $z/\delta_t \approx 10$ can be recovered very deeply inside the boundary layer at positions $z/\delta_t < 0.05$. These correlations are very pronounced. At the edge of the boundary layer at $z/\delta_t \approx 1$ the correlation diminishes, probably due to the high level of stochastic plume activity and the resulting temperature fluctuations interfering the signal with noise.

4. Conclusions

Stimulated by the variety of predictions and experimental observations for the temperature field close to the horizontal plates currently existing, and since data for higher aspect ratios are still missing, we were running a new set of temperature measurements in our large-scale RB facility at $Pr = 0.7$. Extending our previous work [35], we made simultaneous measurements inside and outside the boundary layers of both plates using a redesigned temperature sensor. In particular, we focused in our new experiments on the variation of the aspect ratio keeping the Rayleigh number constant. The experiments covered aspect ratios between $\Gamma = 1.13$ and 2.75 as well as between $\Gamma = 2.75$ and 7.00 at Rayleigh numbers $Ra = 5.2 \times 10^{10}$ and 3.9×10^9 , respectively. In order to enhance the aspect ratio domain an additional experiment at $\Gamma = 9.00$ and $Ra = 1.3 \times 10^9$ has been carried out but the results qualitatively equal the case of $\Gamma = 7.00$.

The main result of our work is that the mean temperature field close to the horizontal plates is virtually not affected by the variation of the aspect ratio and, undoubtedly, the associated transitions in the global flow structure. However, both the total and the normalized boundary-layer thickness δ_t and δ_t/H vary with the aspect ratio, indicating that the Nusselt number depends on this quantity as well. Our refined measurements at both plates along with a quantitative analysis using specific diagnostic functions also show that none of the measured mean temperature profiles includes a significant and long fraction of a linear, logarithmic or power-law dependence with respect to the plate distance. The power law still might be the best fitting function for a limited region $0.05 < z/\delta_t < 0.4$.

Our simultaneously carried out measurements at various distances from both horizontal plates permit us to analyze the dynamics of the evolution of coherent structures in the vicinity of the horizontal plates and the coupling of the boundary layers by these structures. Applying the autocorrelation function to the measured temperature time series, it could be shown that in gases with $Pr = 0.7$ and in the high Rayleigh number regime, plumes are emitted randomly and continuously at all aspect ratios investigated in this work. Periodic oscillations in the temperature signal between $\Gamma = 2$ and 4 obey a cycle time much larger than the typical eddy turnover time. A possible explanation might be that they are induced as the convection rolls change their position with reference to the cell axis. We demonstrated as well that the boundary

layers are decoupled for aspect ratios $\Gamma \leq 2.00$. For higher aspect ratios $\Gamma \geq 4$ they become coupled by small coherent structures evolving close to the plates. Correlations between the temperature fields at the heating and the cooling plates can be evaluated very deeply inside the boundary layer at positions as close as $z/\delta_t = 0.05$ to the plate surface.

Acknowledgments

We acknowledge financial support from the Deutsche Forschungsgemeinschaft under grant number TH 497/22-1 and the Thüringer Ministerium für Bildung, Wissenschaft und Kultur to carry out the study reported in this paper. We thank Philippe Roche for helpful discussions and Vigimantas Mitschunas and Klaus Henschel for their technical help.

References

- [1] Chandrasekhar S 1961 *Hydrodynamic and Hydromagnetic Stability* (Oxford: Clarendon)
- [2] Siggia E D 1994 High Rayleigh number convection *Annu. Rev. Fluid Mech.* **26** 137–68
- [3] Ahlers G, Grossmann S and Lohse D 2009 Heat transfer and large scale dynamics in turbulent Rayleigh–Bénard convection *Rev. Mod. Phys.* **81** 503–37
- [4] Priestley C H B 1957 Convection from the Earth’s surface *Proc. R. Soc. A* **17** 287–304
- [5] Tackley P J 2000 Mantle convection and plate tectonics: toward an integrated physical and chemical theory *Science* **288** 2002–7
- [6] Linden P F 1999 The fluid mechanics of natural ventilation *Annu. Rev. Fluid Mech.* **31** 201–38
- [7] Castaing B, Gunaratne G, Heslot F, Kadanoff L, Libchaber A, Thomae S, Wu X-Z, Zaleski S and Zanetti G P 1989 Scaling of hard thermal turbulence in Rayleigh–Bénard convection *J. Fluid Mech.* **204** 1–30
- [8] Niemela J J and Sreenivasan K R 2003 Confined turbulent convection *J. Fluid Mech.* **481** 355–84
- [9] Roche P-E, Gauthier F, Chabaud B and Hebral B 2005 Ultimate regime of convection: robustness to poor thermal reservoirs *Phys. Fluids* **17** 115107
- [10] Funfschilling D, Bodenschatz E and Ahlers G 2009 Search for the ‘Ultimate State’ in turbulent Rayleigh–Bénard convection *Phys. Rev. Lett.* **103** 014503
- [11] Grossmann S and Lohse D 2000 Scaling in thermal convection: a unifying theory *J. Fluid Mech.* **407** 27–56
- [12] Grossmann S and Lohse D 2002 Prandtl and Rayleigh number dependence of the Reynolds number in turbulent convection *Phys. Rev. E* **66** 016305
- [13] Grossmann S and Lohse D 2003 On geometry effects in Rayleigh–Bénard convection *J. Fluid Mech.* **486** 105–14
- [14] Qiu X-L and Tong P 2001 Large-scale velocity structures in turbulent thermal convection *Phys. Rev. E* **64** 036304
- [15] Resagk C, du Puits R, Thess A, Dolzhansky F V, Grossmann S, Araujo F F and Lohse D 2006 Oscillations of the large scale wind in turbulent thermal convection *Phys. Fluids* **18** 095105
- [16] Brown E and Ahlers G 2006 Rotations and cessations of the large-scale circulation in turbulent Rayleigh–Bénard convection *J. Fluid Mech.* **568** 351–86
- [17] Xi H-D, Zhou Q and Xia K-Q 2006 Azimuthal motion of the mean wind in turbulent thermal convection *Phys. Rev. E* **73** 056312
- [18] Brown E and Ahlers G 2007 Large-scale circulation model for turbulent Rayleigh–Bénard convection *Phys. Rev. Lett.* **98** 134501
- [19] Niemela J J and Sreenivasan K R 2006 Turbulent convection at high Rayleigh numbers and aspect ratio 4 *J. Fluid Mech.* **557** 411–22

- [20] du Puits R, Resagk C and Thess A 2007 Breakdown of wind in turbulent thermal convection *Phys. Rev. E* **75** 016302
- [21] Bailon-Cuba J, Emran M S and Schumacher J 2010 Aspect ratio dependence of heat transfer and large-scale flow in turbulent convection *J. Fluid Mech.* **655** 152–73
- [22] Fleischer A S and Goldstein R J 2002 High-Rayleigh-number convection of pressurized gases in a horizontal enclosure *J. Fluid Mech.* **469** 1–12
- [23] Funfschilling D, Brown E, Nikolaenko A and Ahlers G 2005 Heat transport by turbulent Rayleigh–Bénard convection in cylindrical samples with aspect ratio one and larger *J. Fluid Mech.* **536** 145–54
- [24] Sun C, Ren L-Y, Song H and Xia K-Q 2005 Heat transport by turbulent Rayleigh–Bénard convection in 1 m diameter cylindrical cells of widely varying aspect ratio *J. Fluid Mech.* **542** 165–74
- [25] Zhou Q, Liu B-F, Li C-M and Zhong B-C 2012 Aspect ratio dependence of heat transport by turbulent Rayleigh–Bénard convection in rectangular cells *J. Fluid Mech.* **710** 260–76
- [26] van der Poel E P, Stevens R J A M and Lohse D 2011 Connecting flow structures and heat flux in turbulent Rayleigh–Bénard convection *Phys. Rev. E* **84** 045303
- [27] Daya Z A and Ecke R E 2001 Does turbulent convection feel the shape of the container? *Phys. Rev. Lett.* **87** 184501
- [28] Kaczorowski M and Wagner C 2007 Direct numerical simulation of turbulent convection in a rectangular Rayleigh–Bénard cell *5th Int. Symp. on Turbulence and Shear Flow Phenomena (Garching)* vol 2 pp 499–504
- [29] Song H and Tong P 2010 Scaling laws in turbulent Rayleigh–Bénard convection under different geometry *Europhys. Lett.* **90** 44001
- [30] Fitzjarrald D E 1977 An experimental study of turbulent convection in air *J. Fluid Mech.* **73** 693–719
- [31] Belmonte A, Tilgner A and Libchaber A 1994 Temperature and velocity boundary layers in turbulent convection *Phys. Rev. E* **50** 269–79
- [32] Lui S-L and Xia K-Q 1998 Spatial structure of the thermal boundary layer in turbulent convection *Phys. Rev. E* **57** 5494–503
- [33] Ebert A, Resagk C and Thess A 2008 Experimental study of temperature distribution and local heat flux for turbulent Rayleigh–Bénard convection of air in a long rectangular enclosure *Int. J. Heat Mass Trans.* **51** 4238–48
- [34] Zhou Q, Stevens R J A M, Sugiyama K, Grossmann S, Lohse D and Xia K-Q 2010 Prandtl-Blasius temperature and velocity boundary-layer profiles in turbulent Rayleigh–Bénard convection *J. Fluid Mech.* **664** 297–312
- [35] du Puits R, Resagk C, Tilgner A, Busse F H and Thess A 2007 Structure of thermal boundary layers in turbulent Rayleigh–Bénard convection *J. Fluid Mech.* **572** 231–54
- [36] du Puits R, Resagk C and Thess A 2009 Structure of viscous boundary layers in turbulent Rayleigh–Bénard convection *Phys. Rev. E* **80** 036318
- [37] Grossmann S and Lohse D 2011 Multiple scaling in the ultimate regime of thermal convection *Phys. Fluids* **23** 045108
- [38] Shi N, Emran M S and Schumacher J 2012 Boundary layer structure in turbulent Rayleigh–Bénard convection *J. Fluid Mech.* **706** 5–33
- [39] Prandtl L 1904 Über Flüssigkeitsbewegung bei sehr kleiner Reibung, Verhandlg. III. *Int. Mathematiker Kongresses (Heidelberg, Germany)* pp 484–91
- [40] Blasius H 1908 Grenzschichten in Flüssigkeiten mit kleiner Reibung *Z. Math. Phys.* **56** 1–37
- [41] Pohlhausen E 1921 Der Wärmeaustausch zwischen festen Körpern und Flüssigkeiten mit kleiner Reibung und kleiner Wärmeleitung *Z. Angew. Math. Mech.* **1** 115–21
- [42] Shishkina O and Thess A 2009 Mean temperature profiles in turbulent Rayleigh–Bénard convection of water *J. Fluid Mech.* **633** 449–60
- [43] Stevens R J A M, Zhou Q, Siegfried Grossmann, Verzicco R, Xia K Q and Lohse D 2012 Thermal boundary layer profiles in turbulent Rayleigh–Bénard convection in a cylindrical sample *Phys. Rev. E* **85** 027301

- [44] Townsend A A 1958 Temperature fluctuations over a heated horizontal surface *J. Fluid Mech.* **5** 209–41
- [45] Deardorff J W and Willis G E 1967 Investigation of turbulent thermal convection between horizontal plates *J. Fluid Mech.* **28** 675–704
- [46] Villiermaux E 1995 Memory-induced low frequency oscillations in closed convection boxes *Phys. Rev. Lett.* **75** 4618–21
- [47] Xi H-D, Zhou S-Q, Zhou Q, Chan T-S and Xia K-Q 2009 Origin of the temperature oscillation in turbulent thermal convection *Phys. Rev. Lett.* **102** 044503
- [48] Kaiser R and du Puits R 2012 Error estimation of temperature measurements in non-isothermal shear layers *Exp. Fluids* **53** 137–43
- [49] Scheel J D 2011 private communication
- [50] Resagk C, du Puits R, Maystrenko A, Thess A, Bosbach J and Wagner C 2005 Large-scale particle image velocimetry in convective airflow *6th Int. Symp. on Particle Image Velocimetry (Pasadena)* pp S12–5
- [51] Lobutova E, Resagk C and Putze T 2010 Investigation of large-scale circulations in room air flows using three-dimensional particle tracking velocimetry *Build. Environ.* **45** 1653–62
- [52] Maystrenko A, Resagk C and Thess A 2007 Structure of thermal boundary layer for turbulent Rayleigh–Bénard convection of air in a long rectangular box *Phys. Rev. E* **75** 066303
- [53] du Puits R 2011 Preliminary flow visualization test measurements (unpublished)
- [54] Funfschilling D and Ahlers G 2004 Plume motion and large-scale circulation in a cylindrical Rayleigh–Bénard cell *Phys. Rev. Lett.* **19** 194502
- [55] du Puits R, Resagk C and Thess A 2007 Mean velocity profile in confined turbulent convection *Phys. Rev. Lett.* **99** 234504
- [56] Tilgner A, Belmonte A and Libchaber A 1993 Temperature and velocity profiles of turbulent convection in water *Phys. Rev. E* **47** 2253–6
- [57] du Puits R, Resagk C and Thess A 2010 Measurements of the instantaneous local heat flux in turbulent Rayleigh–Bénard convection *New J. Phys.* **12** 075023